Editors' Suggestion

Interface-Governed Deformation of Nanobubbles and Nanotents Formed by Two-Dimensional Materials

Zhaohe Dai,[1] Yuan Hou,[2] Daniel A. Sanchez,[3] Guorui Wang,[2] Christopher J. Brennan,[4]
Zhong Zhang,[2] Luqi Liu,[2,*] and Nanshu Lu[1,3,4,5,†]
[1]*Center for Mechanics of Solids, Structures and Materials, Department of Aerospace Engineering and Engineering Mechanics, The University of Texas at Austin, Austin, Texas 78712, USA*
[2]*CAS Key Laboratory of Nanosystem and Hierarchical Fabrication, CAS Center for Excellence in Nanoscience National Center for Nanoscience and Technology, Beijing 100190, China*
[3]*Texas Materials Institute, The University of Texas at Austin, Austin, Texas 78712, USA*
[4]*Department of Electrical and Computer Engineering, The University of Texas at Austin, Austin, Texas 78712, USA*
[5]*Department of Biomedical Engineering, The University of Texas at Austin, Austin, Texas 78712, USA*

(Received 27 July 2018; published 26 December 2018)

Nanoblisters such as nanobubbles and nanotents formed by two-dimensional (2D) materials have been extensively exploited for strain engineering purposes as they can produce self-sustained, nonuniform in-plane strains through out-of-plane deformation. However, deterministic measure and control of strain fields in these systems are challenging because of the atomic thinness and unconventional interface behaviors of 2D materials. Here, we experimentally characterize a simple and unified power law for the profiles of a variety of nanobubbles and nanotents formed by 2D materials such as graphene and MoS_2 layers. Using membrane theory, we analytically unveil what sets the in-plane strains of these blisters regarding their shape and interface characteristics. Our analytical solutions are validated by Raman spectroscopy measured strain distributions in bulged graphene bubbles supported by strong and weak shear interfaces. We advocate that both the strain magnitudes and distributions can be tuned by 2D material-substrate interface adhesion and friction properties.

DOI: 10.1103/PhysRevLett.121.266101

Two-dimensional (2D) materials are atomically thin crystals with unique properties that lend well to next-generation ultrathin electronic and optoelectronic devices [1–4]. It has been well established that mechanical strain can strongly perturb the band structure of these materials, giving rise to the possibility of using mechanical deformation to tune their electronic and photonic performance dramatically [5–9]. In fact, this principle, termed strain engineering, is now routinely used in manufacturing traditional semiconductor devices [10]. The strain engineering of 2D materials is particularly exciting because an individual atomic sheet is intrinsically capable of sustaining much larger mechanical strain compared to either their bulk counterparts or conventional electronic materials [11,12]. Also, the atomic thickness of 2D materials allows them to be easily poked or pressurized from the third dimension (i.e., perpendicular to their plane of atoms) [13–17]. The resulting configurations including nanoscale bubbles and tents can be called by a unified name, 2D material blisters [13–20]. Recently, the considerable strain associated with these nanoblisters has created opportunities for the study of new fundamental physics and applications such as enormous pseudomagnetic fields, large-scale quantum emitters, and so on [21–23].

A major challenge in these systems is to find out or even control the strain in the blisters deterministically, calling for understanding and validating how the blister geometry intertwines with mechanics in these atomic sheets [24,25]. So far, self-similar profiles of the 2D material bubbles have been widely discovered in experiments [15,17,26,27]. However, it remains challenging to analytically relate the bubble and tent shape characteristics to the full-field strain distributions and experimentally prove the relation. Consequently, accurate strain tuning through blister shape adjustments is still elusive [21,22,24]. One difficulty comes from the intrinsically nonlinear coupling between in-plane strain and out-of-plane deformations predicted by the membrane theory [28]. More fundamental concern arises from the subtle nature of 2D materials, where the material thickness approaches the atomic scale and the surface is atomically smooth [29]. These features even challenge the applicability of continuum theories from a perspective of deformation physics [30–34]. As a result, the prevailing analysis of the strain distribution and strain-coupled physics and chemistry in 2D material blisters relies heavily on numerical techniques, such as case-by-case molecular dynamics (MD) simulations [22,24,35–37]. To deal with these concerns, a combination of continuum theories with microscale experiments is highly needed and yet to emerge so far.

Herein, we experimentally explore the strain field in nanoblisters formed by 2D materials accounting for

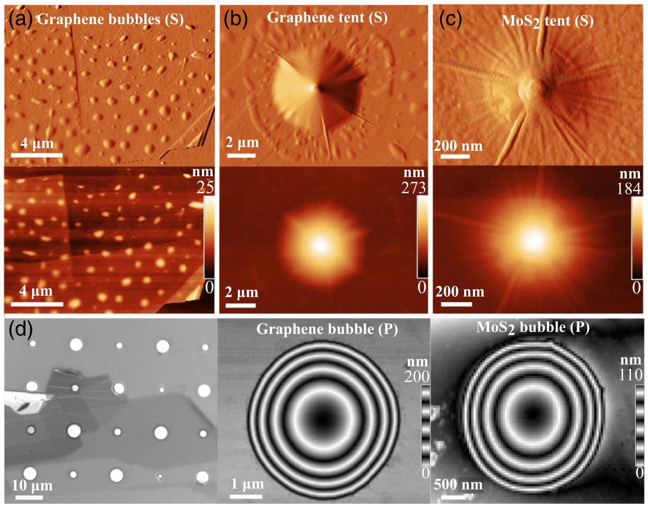

FIG. 1. From top to bottom: Atomic force microscopy (AFM) phase and height images of spontaneously formed graphene bubbles on SiO_2 (a), a multilayer graphene tent on SiO_2 (b), and a CVD-MoS_2 tent on gold film (c). (d) From left to right: optical image of graphene flakes exfoliated on prepatterned SiO_2 with microcavities, AFM height images of a monolayer graphene bubble, and a four-layer MoS_2 bubble. Note that (S) represents bubbles or tents formed spontaneously while (P) represents those formed by controllable air pressurization.

different natures of 2D materials interfaces. Using tapping mode atomic force microscopy (AFM), we experimentally characterized a variety of bubbles and tents formed by graphene and MoS_2 layers. Their shapes were empirically found to follow a simple power law, enabling closed-form analytical solutions to the Föppl–von Kármán equations at the membrane limit. Our results show that the strain distribution in the 2D material can be estimated by simply measuring the height and radius of the bubbles and tents, and that the strain highly depends on the interfacial interaction between the 2D material and the underlying substrate. To validate our analytical solutions, we experimentally carried out Raman mapping on pressurized graphene nanobubbles with strong (graphene-SiO_2) and weak (graphene-graphene) shear interfaces. The measured and analytically predicted Raman shifts have found good matches for both types of interfaces.

We first investigate the shape characteristics of both nanobubbles and nanotents of 2D materials, which can form spontaneously or be created in a controllable manner. For the spontaneous case, nanometer-scale bubbles and tents form when monolayer or few-layer 2D materials are exfoliated or transferred on a target substrate. The formation mechanism is typically attributed to the inevitably trapped water, hydrocarbon, and/or nanoparticles at the 2D material-substrate interface during sample preparation [15,17]. The spontaneously formed nanobubbles and nanotents analyzed in this study were made by mechanically exfoliating few- and monolayer graphene and MoS_2 from their bulk crystals on silicon substrate, or transferring CVD-grown MoS_2 on a gold or Al_2O_3 substrate [38]. Details on the transfer process for different types of samples are provided in the methods section of the Supplemental Material [39]. Figure 1(a) displays typical examples of nanobubbles formed by monolayer graphene on SiO_2. When nanoparticles were trapped, 2D materials can drape around the nanoparticle, forming micro- or nanotents as shown in Figs. 1(b) and 1(c). To form controllable bubbles, we transferred monolayer graphene and a 4-layer MoS_2 to cover prepatterned microcavities in SiO_2 to form suspended drumheads and then followed a well-established gas diffusion procedure to bulge the drumheads [16]. In this case, the bubbles can be pressurized controllably [Fig. 1(d) [39]].

The out-of-plane profiles of all the different types of bubbles and tents prepared by us and collected from the literature are summarized in Fig. 2. Although the radii of the 2D material blisters range from tens to thousands of nanometers, we realized that the height profiles of bubbles and tents collapse onto two master curves if we normalize the out-of-plane deflection (w) of each blister by its central height (h), and the radial positions (r) by its radius (a). We discovered that the collapsed height profiles can be described by a unified power form,

$$\frac{w}{h} = 1 - \left(\frac{r}{a}\right)^{\alpha}, \tag{1}$$

where α is 2 for bubbles or $2/3$ for tents. Note that Fig. 2 summarizes graphene and MoS_2 bubbles and tents with aspect ratios ranging from 0.05 to 0.20. Remarkably, regardless of the aspect ratios, the types of 2D material, the supporting substrates (silicon, alumina, or atomically flat 2D material flakes), the content in the bubble (liquid or gas), or the fabrication methods, all bubble profiles can collapse to Eq. (1) with $\alpha = 2$ [Fig. 2(a)]. We also found that for profiles of graphene and MoS_2 tents, data obtained from MD simulations or coarse-grained (CG) modeling [22,24,36] can also collapse to Eq. (1) with $\alpha = 2/3$ [Fig. 2(b)]. In fact, the empirical conclusion of $\alpha = 2$ is

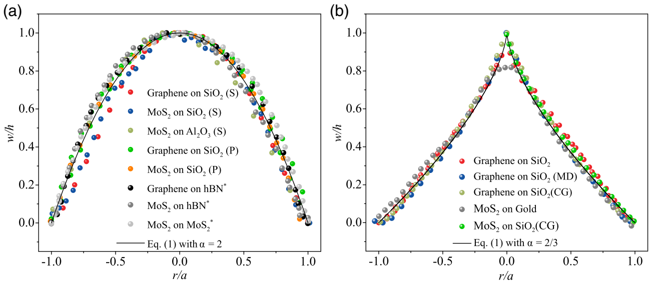

FIG. 2. Universal shape characteristics of 2D material bubbles and tents. (a) Normalized bubble profiles measured by our experiments and collected from literature. Note that samples from Ref. [17] feature atomically smooth interfaces, are labeled by *. (b) Normalized tent profiles measured by our experiments and simulation results in the literature. The simulation data about graphene and MoS_2 is from Refs. [36,24], respectively.

a widely adopted simple membrane solution for blisters [48,49] and $\alpha = 2/3$ is well matched with the analytical solution to an indented blister in the literature [28,50]. We thus conclude that this simple power form can be a good approximation for describing the profiles of 2D material bubbles and tents.

Now that the out-of-plane displacement of 2D material blisters is readily available as given in Eq. (1), we can try to solve the in-plane displacement and then calculate strains out of displacements. Attributing to the atomic thinness of 2D materials, it is sufficient to simply use the membrane limit of the Föppl–von Kármán equations [28,48]. The in-plane equilibrium equation in terms of displacements is therefore

$$\frac{d^2u}{dr^2} + \frac{1}{r}\frac{du}{dr} - \frac{u}{r^2} = -\frac{1-\nu}{2r}\left(\frac{dw}{dr}\right)^2 - \frac{dw}{dr}\frac{d^2w}{dr^2}, \tag{2}$$

where u is the in-plane displacement of the 2D material and ν is the Poisson's ratio. Plugging Eq. (1) into this equation and solving the 2nd order ODE using the finite condition when $r \to 0$ can yield an analytical solution to the in-plane displacement:

$$u = \zeta(\nu)\frac{h^2}{a}\left[\frac{r}{a} - \left(\frac{r}{a}\right)^{2\alpha-1}\right] + u_s\frac{r}{a}, \tag{3}$$

where $\zeta(\nu) = \{[\alpha(2\alpha - 1 - \nu)]/[8(\alpha - 1)]\}$ and u_s is a constant related to the slippage at the edge of the blister ($r = a$). This explicit displacement field allows for the direct solutions for both the radial and circumferential strain fields:

$$\varepsilon_r = \begin{cases} \zeta(\nu)\frac{h^2}{a^2}\left[1 - \frac{1+\nu-2\alpha\nu}{2\alpha-1-\nu}\left(\frac{r}{a}\right)^{2\alpha-2}\right] + \frac{u_s}{a}, & r \le a \\ -\frac{au_s}{r^2}, & r > a \end{cases}, \tag{4a}$$

$$\varepsilon_\theta = \begin{cases} \zeta(\nu)\frac{h^2}{a^2}\left[1 - \left(\frac{r}{a}\right)^{2\alpha-2}\right] + \frac{u_s}{a}, & r \le a \\ \frac{au_s}{r^2}, & r > a \end{cases}. \tag{4b}$$

Clearly, the sliding of the 2D material-substrate interface ($u_s \neq 0$) can induce nonzero strain in the supported zone ($r > a$), which is important for strain engineering applications of 2D materials [35]. Typically, the edge of the 2D material blister is assumed to be fully clamped due to adhesion and strong shear interactions with the supporting substrate outside of boundary [11,22.16]. However, the atomically smooth surfaces of 2D materials make interfacial sliding particularly easy. Recent experiments on gas-pressurized graphene bubbles revealed that the shear interactions between graphene and its substrate can be fairly weak, leading to nonlinear, deflection-dependent interface sliding displacements [14,51]. It has also been discovered that well-established theories assuming clamped conditions offer good approximations only when the deflection is small ($h/a < 0.1$), while experimental measurements deviated from theories with clamped boundaries in samples with large deflection [14]. Recent studies on 2D material interface further highlighted the so-called superlubrication (near-zero friction) when a 2D material sits on atomically smooth substrates, including itself, which is very common in 2D materials devices [52].

Considering that the graphene and MoS_2 blisters in Fig. 2 encompass either relatively strong interfaces with small deflections or atomically lubricated interfaces, our prime interest of this study is in two limits: strong-shear limit (clamped, fully bonded interface) and weak-shear limit (sliding, frictionless interface). For the former, we can apply clamped boundary at the edge of the blister. For the latter, the stress and displacement in the outer supported region can be obtained as the classical Lamé problem in linear elasticity [53]. The stress and displacement continuity then leads to [39]

$$u_s = \begin{cases} 0, & \text{strong-shear limit} \\ -\frac{\alpha(1+v)}{8}\frac{h^2}{a}, & \text{weak-shear limit} \end{cases}. \tag{5}$$

Now Eqs. (4) and (5) combined offer the complete analytical solutions to the strain field in 2D materials forming blisters, with either strong or weak interaction with their substrates. After appropriately choosing the α and u_s according to the specific blister shape and 2D material-substrate interface, one can easily compute the strain distribution inside and outside of a 2D blister by simply measuring its height and radius. We note that a generalized analysis may be performed by accounting for the detailed frictional resistance (e.g., the stick-slip behavior) at the 2D material-substrate interface [54].

In Fig. 3, we plot the strain distributions of the 2D material blister as solid curves using our equations. The strain is normalized by h^2/a^2 such that the distribution will only depend on the interface conditions and material

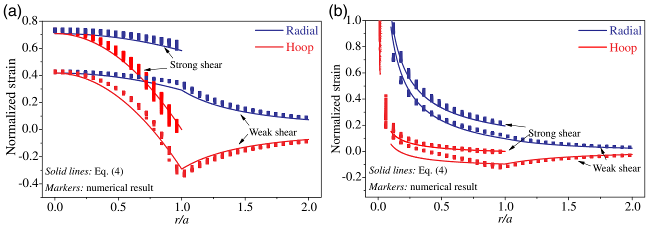

FIG. 3. Normalized strain distribution curves predicted by our analytical solution (solid lines) and solved by numerical analysis (markers) in bubbles (a) and tents (b), subjected to both clamped (strong interface) and frictionless (sliding interfaces) boundary conditions. The strain is normalized by h^2/a^2, giving rise to deflection-independent curves. The numerical results are solved for a monolayer graphene with aspect ratios ranging from $0.02 < h/a < 0.2$.

properties, i.e., the Poisson's ratio. Comparing Fig. 3(a) for bubbles and Fig. 3(b) for tents, it is clear that the strain gradients are much larger in tents, with strain divergence towards the center of the tents due to the assumed point load. Note that under the same aspect ratio, interface sliding can considerably reduce the strain level in 2D material blisters in comparison with blisters with strong-shear interfaces. This highlights the importance of accounting for the ultralubricated interface in the case that the 2D material is supported by an atomically smooth substrate.

Next, we try to verify our analytical solutions numerically. We solved the nonlinear Föppl–von Kármán equations with clamped and slipping boundaries, where the bending behavior is also considered for generality [39]. The numerical solutions are plotted as markers in Fig. 3 for monolayer graphene with aspect ratios ranging from 0.05 to 0.20, to directly compare with the analytical solutions (solid curves). Since analytically solved strains are strictly proportional to h^2/a^2, after normalization, the solid curves are no longer dependent on the aspect ratio. However, the numerically solved strains show more complicated dependence on the aspect ratio, because the markers for different aspect ratios do not fully collapse. Despite this small discrepancy, the overall good agreement between the two solutions indicates that for our experimentally observed blisters with aspect ratios ranging from 0.05 to 0.20, bending effects are negligible. Thus, the numerical results have verified that our analytical solution given by Eq. (4) is a reasonable estimation for strains in both bubbles and tents under both clamped and slipping boundary conditions.

Our analytical solution, though verified numerically, is still challenged by a widespread concern on the breakdown of classical membrane theories at the atomic limit [30–34]. To examine the applicability of our analytical solutions, we performed graphene bulging experiments with intentionally designed strong- and weak-shear interfaces. Monolayer graphene sealed microcavities were fabricated by micromechanical cleavage of graphene over SiO_2 substrate with prepatterned 2.5-micron-radius holes [Fig. 4(a)]. Following a well-developed gas diffusion method [16], we can create a pressure difference across the monolayer and bulge it in a controlled manner.

The strong-shear-interface graphene bubble was generated by pressurizing a graphene monolayer on SiO_2 with the maximum deflection less than 150 nm. Under this condition, the interface sliding was found to be minimal; thus it is compatible with the clamped interface assumption [14]. To experimentally study the weak-shear case, we assembled a graphene-SiO_2 supporting substrate for the graphene bubble [Fig. 4(b)]. First, few-layer graphene was transferred over a SiO_2 microhole. The suspended portion of the multilayer graphene was then etched to open up the microhole. After creating an atomically flat region around the microhole, a monolayer graphene was precisely transferred to cover this microhole, resulting in a graphene drumhead supported by few-layer graphene [39]. Applying a differential pressure across the suspended graphene membrane, this graphene bubble was expected to bulge under weak-shear interface as the graphene-graphene interface can be considered as superlubricated.

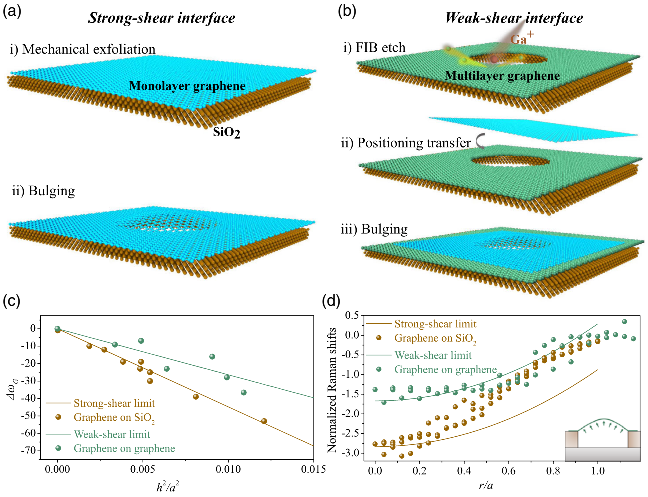

FIG. 4. Schematics of the graphene drumheads formed on a SiO_2 substrate (a) and on a graphene-covered SiO_2 substrate (b). (c) Raman shifts of the G band at the center of graphene bubbles predicted by our analytical solution (solid curves) and measured by our experiments (markers). (d) Normalized Raman shifts of the G band ($\Delta\omega_G a^2/\omega_0 h^2$) as functions of the normalized radial position (r/a) for monolayer graphene bubbles.

We performed multiple AFM and Raman characterizations on the graphene bubbles with well-controlled interfaces [39]. For an axisymmetric graphene bubble, the G band shifts in the Raman spectrum are related to the strain components through the following equation [55]:

$$\frac{\Delta\omega_G}{\omega_0} = -\gamma(\varepsilon_r + \varepsilon_\theta) \pm \frac{\beta}{2}(\varepsilon_r - \varepsilon_\theta), \tag{6}$$

where ε_r and ε_θ are analytically expressed in Eq. (4), γ is the Grüneisen parameter, and β is the shear deformation potential that details the amount of splitting in the G bands, which were experimentally calibrated for monolayer graphene ($\gamma = 1.99$ and $\beta = 0.99$) [56]. Therefore, analytical prediction for strain fields can be readily converted to analytical prediction for the G band shifts using Eq. (6). Particularly, at the center of the bubble where $\varepsilon_r = \varepsilon_\theta$, the G band shifts are predicted by Eqs. (4) and (6) to take a very simple form:

$$\Delta\omega_G = -c\gamma\omega_0 \frac{h^2}{a^2} \tag{7}$$

where the constant c is $[(3-\nu)/2]$ for bubbles supported by strong shear interfaces and is $(1-\nu)$ by weak shear interfaces.

Because of space limitations, we present the details of the experimental Raman characterizations in the Supplemental Material, Note 2 [39]. Here, we first show the

Raman G band shifts at the center of graphene bubbles as a function of h^2/a^2 in Fig. 4(c), which is predicted to be linear by our analytical solution in Eq. (8). The markers represent experimental data for both SiO_2- (brown) and graphene-supported (green) graphene bubbles and the solid curves correspond to predicted G band shifts for strong- (green) and weak-shear-interfaced (brown) 2D material bubbles. By setting the Poisson's ratio of graphene to be 0.165 in Eq. (7), we find good agreement between our theoretical predictions and experimental measurements. This may confirm the applicability of our simplified membrane theory in relating the out-of-plane deformations to in-plane strains for 2D material blisters.

In Fig. 4(d), we further normalize both the measured and predicted G band shifts by h^2/a^2 and plot them as functions of the normalized radial position r/a. Our weak-shear and strong-shear model can partially capture the full-field strain distribution in graphene-on-graphene and graphene-on-SiO_2 bubbles, respectively. However, deviation between predicted and measured G band shifts occurs and enlarges towards the edge of the bubble, especially for SiO_2-supported graphene bubbles. We attribute such edge deviation in Fig. 4(d) to the limited spatial resolution of Raman spectroscopy ($\sim 1\ \mu m$) and the possible doping effect by the substrate [57,58], which are further elucidated in Figs. S9 and S10 [39]. As for 2D material tents, a recent study reported the Raman 2D band shifts for a SiN/Si-supported graphene drumhead subjected to nanoindentation [59]. The experimental results can be well captured by our analytical solution to a 2D material tent with strong-shear interface (Fig. S11 [39]). We thus claim that our analytical solutions in Eq. (5), enabled by the shape characteristics in Fig. 2, can offer valid estimation for the in-plane strain in 2D material bubbles and tents simply by knowing their height and radius. It is especially true at the center of bubbles by Eq. (7), which may, in turn, be used to measure the Grüneisen parameter for the broadly extended 2D material family.

The 2D material bubble and tent structures have been exploited in many recent studies [17–22,27,60–64] where people typically use prepatterned micropillars or interface-confined contents to produce a single or an array of 2D material blisters. Our findings show that the strain in blisters highly hinges on their aspect ratio (h/a). We note that a balance between adhesion (which favors large areas of contact) and stretching energy (which diminishes in blisters of large radius) dictates a constant aspect ratio:

$$h/a = (\phi \Delta\gamma / E_{2D})^{1/4}. \tag{8}$$

where $\Delta\gamma$ is energy change per unit area, E_{2D} is the in-plane stiffness of the 2D material, and ϕ is a constant prefactor. Equation (8) implies that the aspect ratio or ultimately the strain of a 2D material bubble or tent is dominated by the ratio of the 2D material-substrate adhesion to the in-plane stiffness of the 2D material. In fact, this interface- and stiffness-dependent out-of-plane deformation characteristic has been observed at a variety of length scales—from graphene to polymer films with thicknesses ranging from 1 nm to 1 mm [50]. Here, we determine ϕ for 2D material bubbles and tents of both strong- and weak-shear interfaces in Table I [39]. Notably, recent experimental discovery of the constant aspect ratio of 2D material bubbles for a given 2D material-substrate system provided a good validation [17], and there is no available experimental data for 2D material tents so far.

TABLE I. The prefactor ϕ that determines the aspect ratio by $\boldsymbol{\Delta\gamma/E_{2D}}$ in Eq. (8).

Shape		Strong shear	Weak shear
Bubble	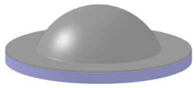	$\{[24(1-\nu)]/[5(7-\nu)]\}$	$(6/5)$
Tent	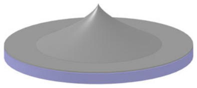	$\{[72(1-\nu)]/[5-3\nu]\}$	18

This work is supported by the NSF Division of Civil, Mechanical and Manufacturing Innovation (CMMI) under Grant No. 1351875, the CNS Catalyst Grant at the University of Texas at Austin, and the National Natural Science Foundation of China (Grant No. 21474023). Z. D. acknowledges Dr. Peng Wang and Professor Rui Huang (UT Austin) for their assistance in numerical method.

[*] To whom all correspondence should be addressed.
liulq@nanoctr.cn
[†] To whom all correspondence should be addressed.
nanshulu@utexas.edu

[1] R. Mas-Balleste, C. Gomez-Navarro, J. Gomez-Herrero, and F. Zamora, Nanoscale **3**, 20 (2011).
[2] K. S. Novoselov, A. Mishchenko, A. Carvalho, and A. H. Castro Neto, Science **353**, aac9439 (2016).
[3] D. Akinwande, N. Petrone, and J. Hone, Nat. Commun. **5**, 5678 (2014).
[4] C. Choi *et al.*, Nat. Commun. **8**, 1664 (2017).
[5] D. Lloyd, X. Liu, J. W. Christopher, L. Cantley, A. Wadehra, B. L. Kim, B. B. Goldberg, A. K. Swan, and J. S. Bunch, Nano Lett. **16**, 5836 (2016).
[6] A. Branny, S. Kumar, R. Proux, and B. D. Gerardot, Nat. Commun. **8**, 15053 (2017).
[7] H. Li *et al.*, Nat. Commun. **6**, 7381 (2015).
[8] G. G. Naumis, S. Barraza-Lopez, M. Oliva-Leyva, and H. Terrones, Rep. Prog. Phys. **80**, 096501 (2017).
[9] G. da Cunha Rodrigues, P. Zelenovskiy, K. Romanyuk, S. Luchkin, Y. Kopelevich, and A. Kholkin, Nat. Commun. **6**, 7572 (2015).
[10] J. A. Del Alamo, Nature (London) **479**, 317 (2011).
[11] C. Lee, X. Wei, J. W. Kysar, and J. Hone, Science **321**, 385 (2008).

[12] C. Androulidakis, K. Zhang, M. Robertson, and S. H. Tawfick, 2D Mater. **5**, 032005 (2018).

[13] D. Davidovikj, F. Alijani, S. Cartamil-Bueno, H. Zant, M. Amabili, and P. Steeneken, Nat. Commun. **8**, 1253 (2017).

[14] G. Wang, Z. Dai, Y. Wang, P. H. Tan, L. Liu, Z. Xu, Y. Wei, R. Huang, and Z. Zhang, Phys. Rev. Lett. **119**, 036101 (2017).

[15] D. A. Sanchez, Z. Dai, P. Wang, A. Cantu-Chavez, C. J. Brennan, R. Huang, and N. Lu, Proc. Natl. Acad. Sci. U.S.A. **115**, 7884 (2018).

[16] S. P. Koenig, N. G. Boddeti, M. L. Dunn, and J. S. Bunch, Nat. Nanotechnol. **6**, 543 (2011).

[17] E. Khestanova, F. Guinea, L. Fumagalli, A. K. Geim, and I. V. Grigorieva, Nat. Commun. **7**, 12587 (2016).

[18] A. Reserbat-Plantey *et al.*, Nano Lett. **14**, 5044 (2014).

[19] H. Tomori, A. Kanda, H. Goto, Y. Ootuka, K. Tsukagoshi, S. Moriyama, E. Watanabe, and D. Tsuya, Appl. Phys. Express **4**, 075102 (2011).

[20] J. M. Lee *et al.*, Nano Lett. **10**, 2783 (2010).

[21] N. Levy, S. Burke, K. Meaker, M. Panlasigui, A. Zettl, F. Guinea, A. C. Neto, and M. Crommie, Science **329**, 544 (2010).

[22] N. N. Klimov, S. Jung, S. Zhu, T. Li, C. A. Wright, S. D. Solares, D. B. Newell, N. B. Zhitenev, and J. A. Stroscio, Science **336**, 1557 (2012).

[23] C. Palacios-Berraquero, D. M. Kara, A. R.-P. Montblanch, M. Barbone, P. Latawiec, D. Yoon, A. K. Ott, M. Loncar, A. C. Ferrari, and M. Atatüre, Nat. Commun. **8**, 15093 (2017).

[24] J. Feng, X. Qian, C.-W. Huang, and J. Li, Nat. Photonics **6**, 866 (2012).

[25] D. Vella and B. Davidovitch, Soft Matter **13**, 2264 (2017).

[26] G. Zamborlini, M. Imam, L. L. Patera, T. O. Menteş, N. Stojić, C. Africh, A. Sala, N. Binggeli, G. Comelli, and A. Locatelli, Nano Lett. **15**, 6162 (2015).

[27] H. Ghorbanfekr-Kalashami, K. S. Vasu, R. R. Nair, F. M. Peeters, and M. Neek-Amal, Nat. Commun. **8**, 15844 (2017).

[28] E. H. Mansfield, *The Bending and Stretching of Plates* (Cambridge University Press, Cambridge, England, 2005).

[29] X. Li, L. Tao, Z. Chen, H. Fang, X. Li, X. Wang, J.-B. Xu, and H. Zhu, Appl. Phys. Rev. **4**, 021306 (2017).

[30] G. López-Polín, C. Gómez-Navarro, V. Parente, F. Guinea, M. I. Katsnelson, F. Pérez-Murano, and J. Gómez-Herrero, Nat. Phys. **11**, 26 (2015).

[31] L. Tapasztó, T. Dumitrică, S. J. Kim, P. Nemes-Incze, C. Hwang, and L. P. Biró, Nat. Phys. **8**, 739 (2012).

[32] J. H. Los, A. Fasolino, and M. I. Katsnelson, Phys. Rev. Lett. **116**, 015901 (2016).

[33] R. J. T. Nicholl, N. V. Lavrik, I. Vlassiouk, B. R. Srijanto, and K. I. Bolotin, Phys. Rev. Lett. **118**, 266101 (2017).

[34] D.-B. Zhang, E. Akatyeva, and T. Dumitrică, Phys. Rev. Lett. **106**, 255503 (2011).

[35] Z. Qi, A. L. Kitt, H. S. Park, V. M. Pereira, D. K. Campbell, and A. H. Castro Neto, Phys. Rev. B **90**, 125419 (2014).

[36] S. Zhu, Y. Huang, N. N. Klimov, D. B. Newell, N. B. Zhitenev, J. A. Stroscio, S. D. Solares, and T. Li, Phys. Rev. B **90**, 075426 (2014).

[37] Z. Meng, R. A. Soler-Crespo, W. Xia, W. Gao, L. Ruiz, H. D. Espinosa, and S. Keten, Carbon **117**, 476 (2017).

[38] Y. Huang, E. Sutter, N. N. Shi, J. Zheng, T. Yang, D. Englund, H. J. Gao, and P. Sutter, ACS Nano **9**, 10612 (2015).

[39] See Supplemental Material at http://link.aps.org/supplemental/10.1103/PhysRevLett.121.266101 for material preparations, experimental setup, and characterizations, and analysis based on membrane mechanics, which includes Refs. [40–47].

[40] C. J. Brennan, R. Ghosh, K. Koul, S. K. Banerjee, N. Lu, and E. T. Yu, Nano Lett. **17**, 5464 (2017).

[41] R. Frisenda, E. Navarro-Moratalla, P. Gant, D. Perez De Lara, P. Jarillo-Herrero, R. V. Gorbachev, and A. Castellanos-Gomez, Chem. Soc. Rev. **47**, 53 (2018).

[42] Y. Zhang, C. Hui, R. Sun, K. Li, K. He, X. Ma, and F. Liu, Nanotechnology **25**, 135301 (2014).

[43] L. G. Cancado, A. Jorio, E. H. Martins Ferreira, F. Stavale, C. A. Achete, R. B. Capaz, M. V. O. Moutinho, A. Lombardo, T. S. Kulmala, and A. C. Ferrari, Nano Lett. **11**, 3190 (2011).

[44] A. C. Ferrari, Solid State Commun. **143**, 47 (2007).

[45] C. Metzger, S. Rémi, M. Liu, S. V. Kusminskiy, A. H. Castro Neto, A. K. Swan, and B. B. Goldberg, Nano Lett. **10**, 6 (2010).

[46] Z. H. Ni, T. Yu, Y. H. Lu, Y. Y. Wang, Y. P. Feng, and Z. X. Shen, ACS Nano **2**, 2301 (2008).

[47] K. M. Yue, W. Gao, R. Huang, and K. M. Liechti, J. Appl. Phys. **112**, 083512 (2012).

[48] L. B. Freund and S. Suresh, *Thin Film Materials: Stress, Defect Formation and Surface Evolution* (Cambridge University Press, Cambridge, England, 2004).

[49] P. Wang, W. Gao, Z. Cao, K. M. Liechti, and R. Huang, J. Appl. Mech. **80**, 040905 (2013).

[50] J. Chopin, D. Vella, and A. Boudaoud, Proc. R. Soc. A **464**, 2887 (2008).

[51] A. L. Kitt, Z. Qi, S. Rémi, H. S. Park, A. K. Swan, and B. B. Goldberg, Nano Lett. **13**, 2605 (2013).

[52] O. Hod, M. Urbakh, D. Naveh, M. Bar-Sadan, and A. Ismach, Adv. Mater. **30**, 1706581 (2018).

[53] M. H. Sadd, *Elasticity: Theory, Applications, and Numerics* (Academic Press, Burlington, MA, 2009).

[54] Q. Li, C. Lee, R. W. Carpick, and J. Hone, Phys. Status Solidi B **247**, 2909 (2010).

[55] M. Huang, H. Yan, C. Chen, D. Song, T. F. Heinz, and J. Hone, Proc. Natl. Acad. Sci. U.S.A. **106**, 7304 (2009).

[56] T. M. G. Mohiuddin,, A. Lombardo, R. R. Nair, A. Bonetti, G. Savini, R. Jalil, N. Bonini, D. M. Basko, C. Galiotis, N. Marzari, K. S. Novoselov, A. K. Geim, and A. C. Ferrari, Phys. Rev. B **79**, 205433 (2009).

[57] J. E. Lee, G. Ahn, J. Shim, Y. S. Lee, and S. Ryu, Nat. Commun. **3**, 1024 (2012).

[58] A. Das *et al.*, Nat. Nanotechnol. **3**, 210 (2008).

[59] K. Elibol, B. C. Bayer, S. Hummel, J. Kotakoski, G. Argentero, and J. C. Meyer, Sci. Rep. **6**, 28485 (2016).

[60] K. Xu, P. Cao, and J. R. Heath, Science **329**, 1188 (2010).

[61] K. Vasu *et al.*, Nat. Commun. **7**, 12168 (2016).

[62] Z. Chen *et al.*, Nat. Commun. **8**, 14548 (2017).

[63] Y. Jiang, J. Mao, J. Duan, X. Lai, K. Watanabe, T. Taniguchi, and E. Y. Andrei, Nano Lett. **17**, 2839 (2017).

[64] D. Akinwande *et al.*, Extreme Mech. Lett. **13**, 42 (2017).

Supplementary Material

Interface-Governed Deformation of Nanobubbles and Nanotents formed by Two-Dimensional Materials

Zhaohe Dai [1], Yuan Hou [2], Daniel A. Sanchez [3], Guorui Wang [2], Christopher J. Brennan [4], Zhong Zhang [2], Luqi Liu [2], Nanshu Lu [1, 3, 4, 5]

[1] *Center for Mechanics of Solids, Structures and Materials, Department of Aerospace Engineering and Engineering Mechanics, The University of Texas at Austin, Austin, Texas 78712, USA.*

[2] *CAS Key Laboratory of Nanosystem and Hierarchical Fabrication, CAS Center for Excellence in Nanoscience National Center for Nanoscience and Technology, Beijing 100190, China.*

[3] *Texas Materials Institute, The University of Texas at Austin, Austin, Texas 78712, USA.*

[4] *Department of Electrical and Computer Engineering, The University of Texas at Austin, Austin, Texas, 78712, USA.*

[5] *Department of Biomedical Engineering, The University of Texas at Austin, Austin, Texas, 78712, USA.*

Correspondence and requests for materials should be addressed to Nanshu Lu (email: nanshulu@utexas.edu) or to Luqi Liu (email: liulq@nanoctr.cn).

The purpose of this supplementary material is to provide detailed experimental data, derivations of the equations discussed in the manuscript, and the numerical method used for solving the Föppl–von Kármán equations. In Note 1, we present detailed experimental data for the fabrication and characterization of graphene bubble and MoS_2 bubble. In Note 2, we present the strain-related Raman analysis of our graphene bubbles. In Note 3, we present how the sliding displacement at the edge of the blister relates to the out-of-plane deformation inside the blister, i.e. Eq. (5) from the main text. In Note 4, we numerically solve the governing equations for a pressurized membrane (bubble) and a point-loaded membrane (tent) with clamped and sliding boundary conditions. In Note 5, we derive the relation between the work of adhesion and the aspect ratio of the nanoblister.

Supplementary Material Note 1

Fabrication of spontaneously formed graphene and MoS_2 blisters. The same exfoliation procedure is used for both HOPG and MoS_2 crystals. Blue polyethylene cleanroom tape (CRT) was used to peel large and thick flake off the bulk crystal. The exfoliated flakes were then brought into contact with another piece of the CRT and exfoliated three more times. The flakes were then stored for a minimum of 3 hours in ambient conditions to allow ambient moisture and other contents to adsorb on the surface of the exposed flakes. The 300 nm SiO_2/Si substrate wafer was first prepared by cutting a 1 cm × 1 cm chip from the wafer. To maximize the area of monolayer regions that were transferred to SiO_2, the SiO_2 chip was exposed to O_2 plasma to remove any organic residue. Immediately after O_2 plasma exposure, the exfoliated HOPG flakes on CRT were placed onto the surface of the SiO_2 chip. Then the SiO_2 chip was placed on a hot plate and was heated at 100°C for two minutes. The sample was removed from the hot plate and cooled to room temperature, after which the CRT was removed. The MoS_2 on Al_2O_3 sample in this work is a different location on the same sample as used in a previous work, where the fabrication and characterization details can be found[1].

Fabrication of air-pressurized MoS_2 bubbles. MoS_2 bubbles were prepared by micromechanical cleavage of a 4-layer MoS_2 sheet on pre-patterned silicon substrates. The substrate was covered with a 300 nm thick SiO_2 layer. An array of round holes was fabricated by photolithography and reactive ion etching, resulting in a depth of 300 nm and a diameter of 3 μm. The lateral dimension was measured by AFM. The samples were placed into a pressure chamber to establish a pressure difference across the graphene membrane, and the accuracy of the gauge was 0.01 MPa. (see Supplementary Fig. S1 for more details)

Fabrication of air-pressurized graphene bubbles. Few- and single- layer graphene were prepared by micromechanical cleavage on the substrates where an array of 5-μm-diameter holes was patterned. The lateral dimension of the monolayer graphene sheet was measured by the optical microscopy, and its monolayer thickness was identified by Raman spectroscopy. Monolayer graphene bubble supported by the silicon substrate (strong-shear interface) was made by following the air-pressurizing process. For monolayer graphene bubble supported by the few-layer graphene (weak-shear interface), a FIB system (FEI 235 DualBeam) was also used to etch few-layer graphene without using masks, giving a resolution of 20 nm. The suspended part of the graphene few-layer was etched to expose the SiO_2 micro-holes, and then a graphene monolayer was transferred on the top of the perforated multilayer. (see Supplementary Fig. S2 for more details). In efforts to avoid the sample variation regarding the graphene-substrate interaction, we prepared multiple samples, especially for the SiO_2-supported case. Specifically, we made four SiO_2-supported samples to provide bubbles with nine different heights. Preparation procedures are relatively challenging and tedious for graphene-supported bubbles. We successfully made three graphene-supported samples which provided bubbles with six different heights.

Characterization of Graphene bubbles. AFM (Dimension Icon, Veeco) in the standard tapping mode was utilized to measure the shape of the graphene bubbles, including the maximum deflection and the radius. We also scanned the profiles of MoS_2 bubbles and tents and graphene tents in the main text, where are captured by Eq. (1). Note that for the tent case, the Eq. (1) can be used as a fitting function. High-frequency Raman measurements were performed using an Invo-Renishaw system with an incident wavelength of 532 nm from a diode-pumped solid-state laser. The spectral resolution was 1.0 $cm^{-1,}$ and the spatial resolution was ∼1 μm. The laser intensity was kept below 0.5 mW to avoid local heating induced by the laser. For the Raman scanning under various heights, Raman spectra from every spot of the sample were recorded with the step size of 100 nm. All featured bands in Raman spectra of graphene were fitted with Lorentzian functions to obtain the peak positions.

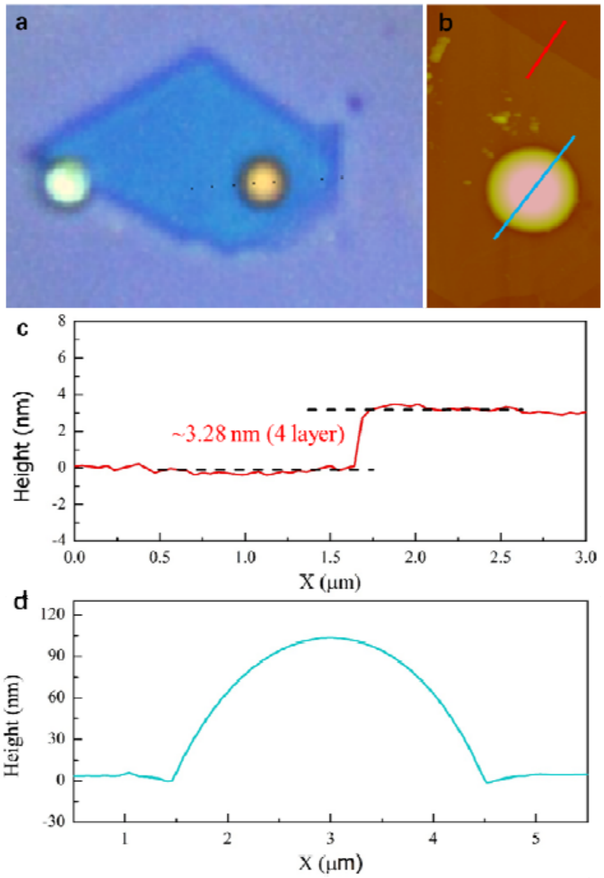

Figure S1 | Fabrication and characterization of an air-pressurized MoS_2 bubble. (**a**) Optical microscopy image of MoS_2 flake deposited on a micro-hole with a diameter of 3 µm. (**b**) AFM image of a MoS_2 bubble at the applied pressure of 0.5 MPa. The graphs correspond to the topographic profiles along the red line and blue line in the AFM image showing (**c**) flake thickness and (**d**) bubble height.

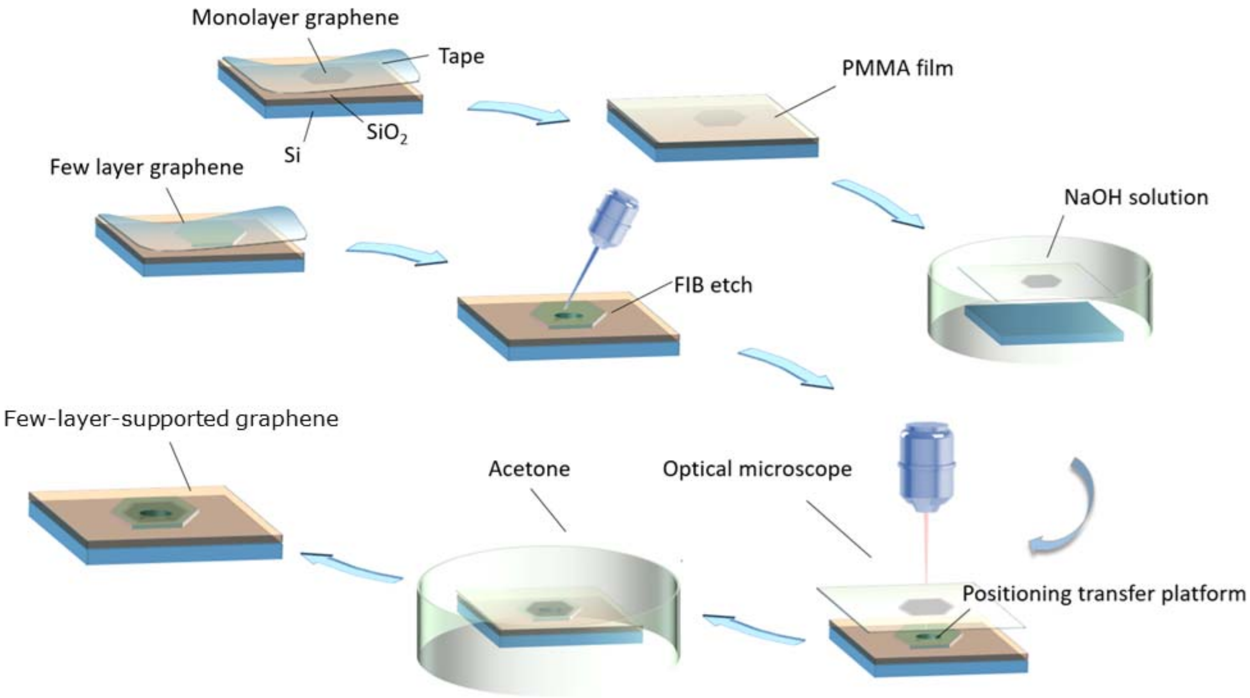

Figure S2 | Fabrication process of a multilayer structure. A FIB system (FEI 235 DualBeam) was also used to etch few-layer graphene without using masks, giving a resolution of 20 nm. The suspended part of the graphene multilayer was etched to expose the SiO_2 mirco-holes, and then a graphene monolayer was transferred on the top of the perforated multilayer. (see Supplementary Information Fig. S2 for more details) The beam current was 1 pA to ensure the integrity of graphene. Then the few-layer graphene was annealed at 200°C in both Ar and H_2 processes for 2h to minimize the number of defects. A thin layer (200 nm) of poly(methyl methacrylate) (PMMA) resist was then spin-coated on to a substrate containing the desired graphene and subsequently heated at 120 ℃ for 12 min to evaporate the solvent from the resist. An adhesive tape window was placed above the PMMA layer, ensuring that the desired graphene flake was at the center of the open area. The entire sample was then placed in 3% NaOH solution to etch away the SiO_2 layer and thereby the tape window with the PMMA layer containing the graphene flake floated on the surface of the NaOH solution due to the hydrophobic nature of PMMA, whereas the Si substrate stays at the bottom. Subsequently, the tape window holding the graphene-PMMA layer was rinsed with deionized water to remove any residual NaOH solution. After 12h drying, the graphene-PMMA layer was attached to the hollow metal frame, and then the positioning transfer stage was used to locate the monolayer graphene on the top of the graphene substrate using the optical microscopy. Finally, the samples were heated to 150 ℃ for 3h, and the top PMMA layer was removed using an acetone wash[2].

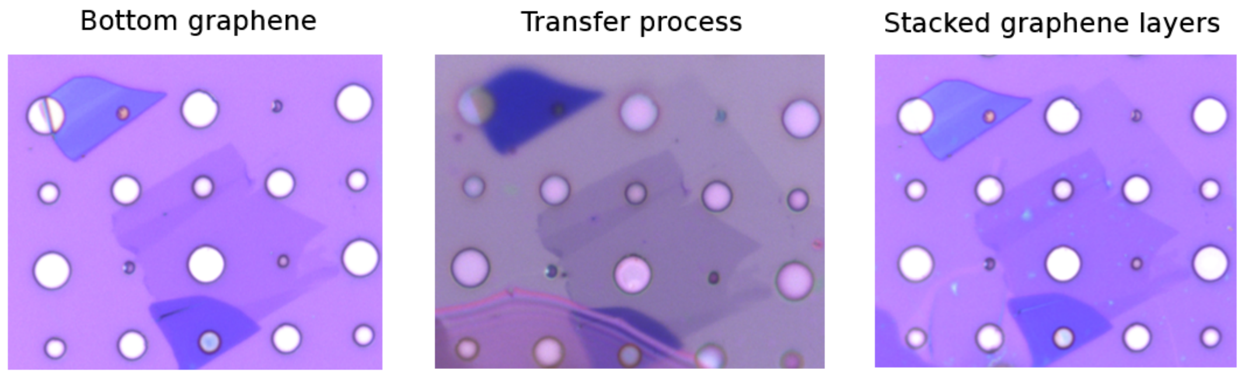
Bottom graphene

Transfer process

Stacked graphene layers

Figure S3 | Optical images of our multilayer structure. From left to right: etched bottom few-layer graphene on SiO_2, positioning transfer of the top monolayer graphene on the bottom one, final configuration of the multilayer structure. The diameter of large holes is 5 μm.

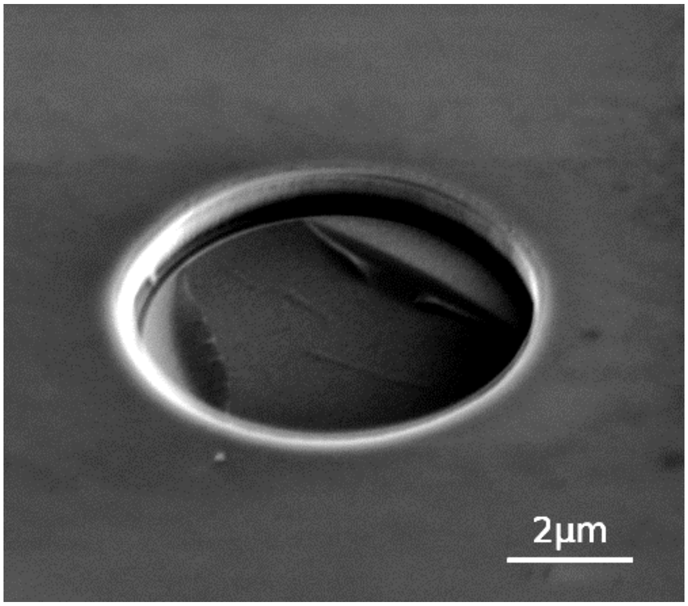

Figure S4 | SEM of the FIB-etched few-layer graphene. A focused ion beam (Ga^+ ions, FIB – NOVA 200 Nanolab – FEI Co.) were used to fabricate the multilayer graphene substrate. To minimize the influence of radiation, the processing parameters were set as operated at 30 kV, 1PA and an annealing treatment were also performed after FIB etching[3].

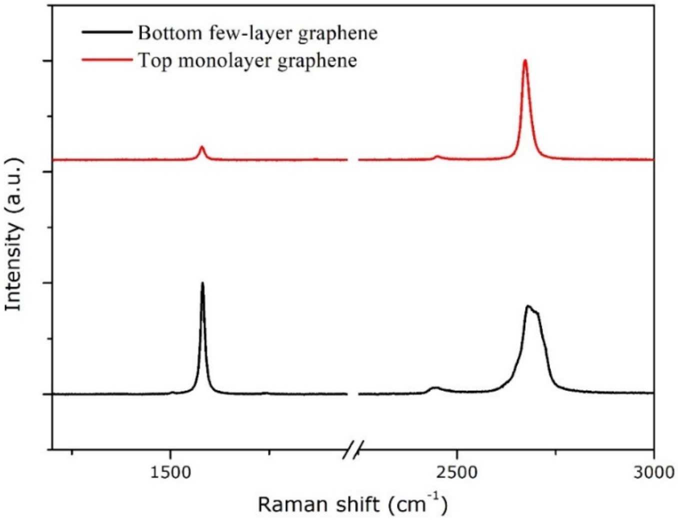

Figure S5 | Raman characterization of the bottom and top layer graphene. The layer numbers of graphene layers were identified by Invo-Renishaw system via the intensity ratio of G-band and 2D -band. Here, the layer numbers of bottom graphene were determined to be three layers.

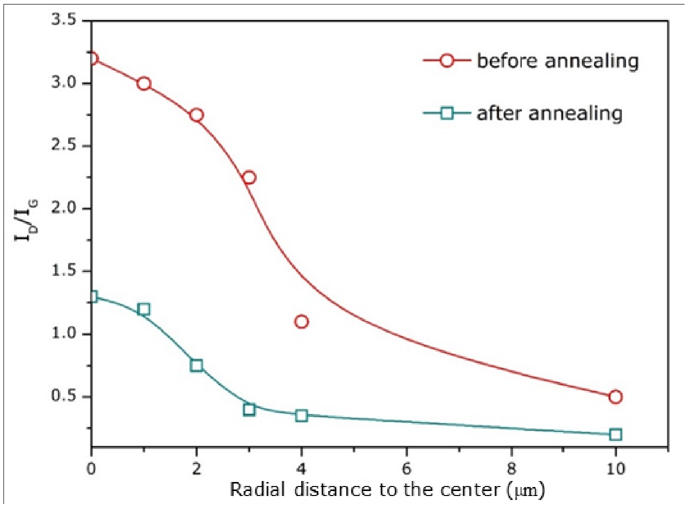

Figure S6 | Annealing FIB-etched graphene to reduce the defects. Compared with pristine graphene having G-band and 2D-band, D-band and D′ -band occurred with Raman double resonance process induced by vacancy defects (caused by the bombardment of Ga$^+$) in graphene structure. Both the Raman D-band and D′ -band are enhanced simultaneously with increasing irradiation time. Here, the Raman intensity ratio I_D/I_G is proportional to the defect concentration at low defect density[4].

Supplementary Material Note 2

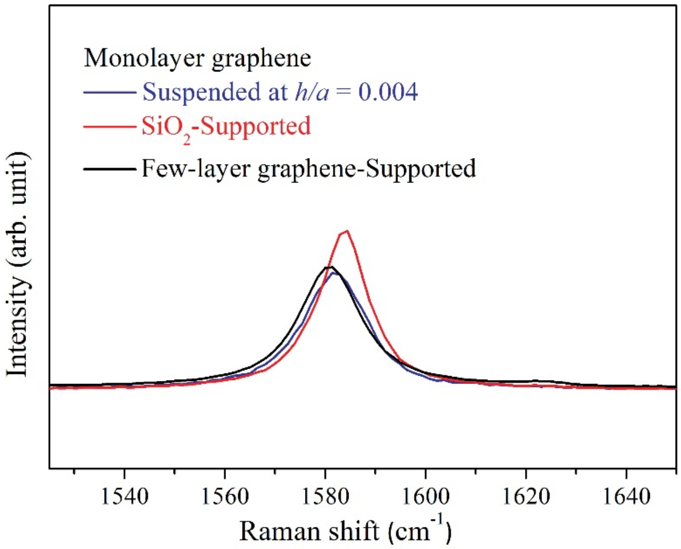

Figure S7 | Representative Raman spectra obtained from the SiO_2-supported graphene (red line), graphene-supported graphene, and the suspended graphene with *h/a* = 0.004 (blue line). Compared with those measured at the center of the suspended graphene with near zero deformation, the Raman G bands measured at SiO_2-supported and graphene-supported monolayer graphene are upshifted by 2-4 cm^{-1} and downshifted by 0-2 cm^{-1}, respectively. Such variations in Raman modes are mainly stemmed from doping effect by SiO_2 substrate [5]. In the main text, we used the center of suspended graphene with nearly zero deformation ($h/a = 0.004, h^2/a^2 = 1.6 \times 10^{-5}$) as the zero-strain reference since we are dealing with the suspended part of the graphene bubble. However, the doping effect may cause errors in the strain calculation of bubbles (especially formed by SiO_2-supported graphene) that are close to the edge (the substrate). This may explain the deviation between our theoretical predictions and experimental measurements in Figure 4d in the main text.

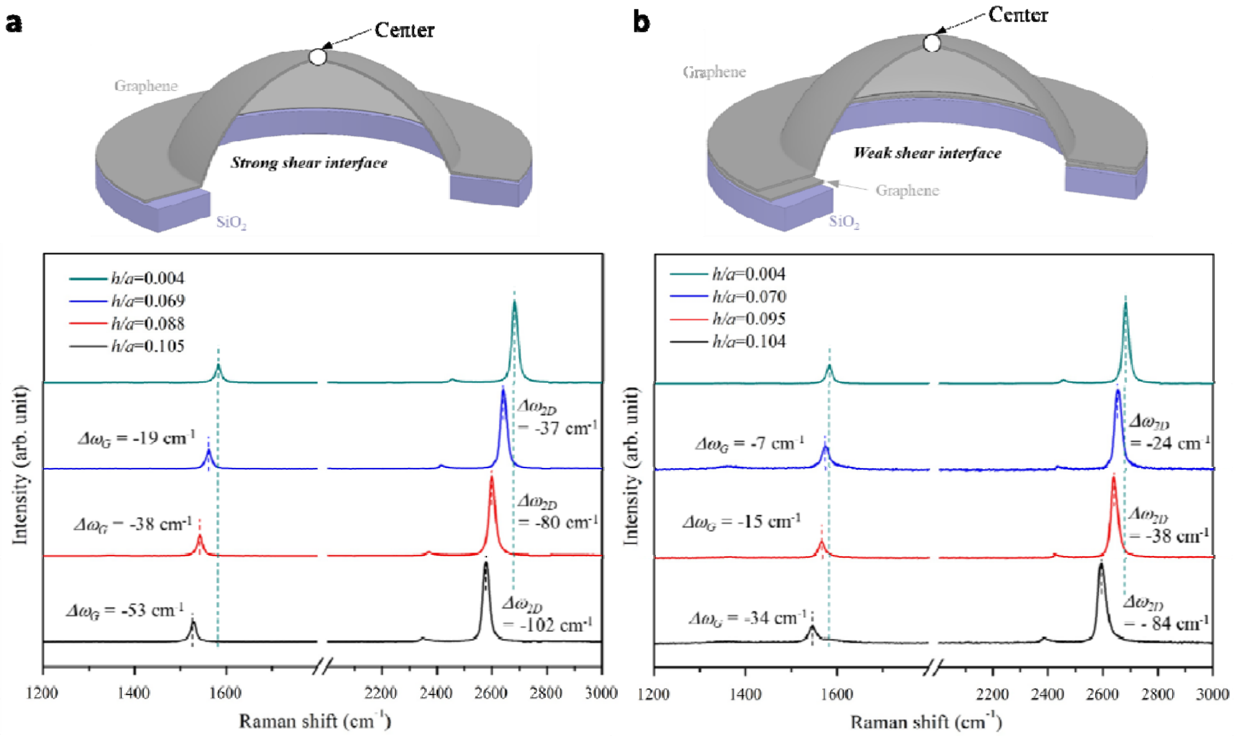

Figure S8 | Representative Raman spectra measured at the center of the graphene bubble under different levels of deformation (*h/a*). (**a**) SiO$_2$-supported graphene bubbles. (**b**) Graphene-supported graphene bubbles. We note that when subjected to equal deformation level, SiO$_2$-supported graphene bubbles exhibit much more significant G and 2D band shifts than graphene-supported graphene bubbles. Specifically, when the *h/a* ≈ 0.1, the G band downshifted by 53 and 34 cm^{-1} for the SiO$_2$-supported and the graphene-supported graphene bubble, respectively. And the 2D band downshifted by 102 and 84 cm^{-1} for the SiO$_2$-supported and the graphene-supported graphene bubble, respectively. This fact implies that the sliding behavior of graphene-graphene interface at the edge can considerably reduce the strain magnitude in the bubble.

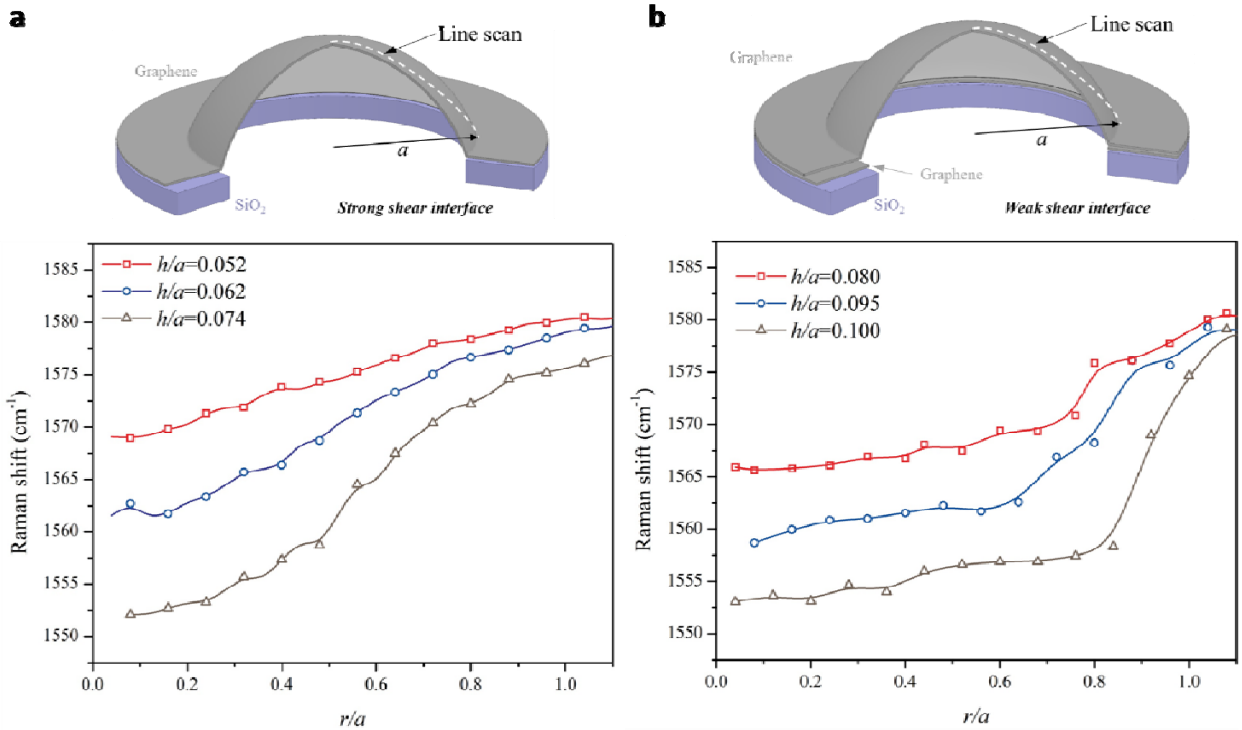

Figure S9 | Line mapping of Raman G band frequency. (**a**) SiO_2-supported graphene bubbles. (**b**) Graphene-supported graphene bubbles. Unsurprisingly, the Raman G band shifts increase with the applied out-of-plane deformation. Also, the shifts decrease from the center (r/a = 0) to the edge (r/a = 1) of the bubble, implying that the "strain" increases from the edge to the center. When approaching the edge, the curves of Raman G band shift (as functions of the radial position) behave differently between SiO_2-supported and graphene-supported graphene bubbles. One possible reason likely comes from the different doping levels by the substrate, which is SiO_2 for (a) and few-layer graphene for (b). For instance, in Fig. S7, we found the upshifting of G band with 2-4 cm^{-1} by the SiO_2 doping while the downshifting of G band with 0-2 cm^{-1} by the hybrid substrate doping (few-layer graphene on SiO_2).

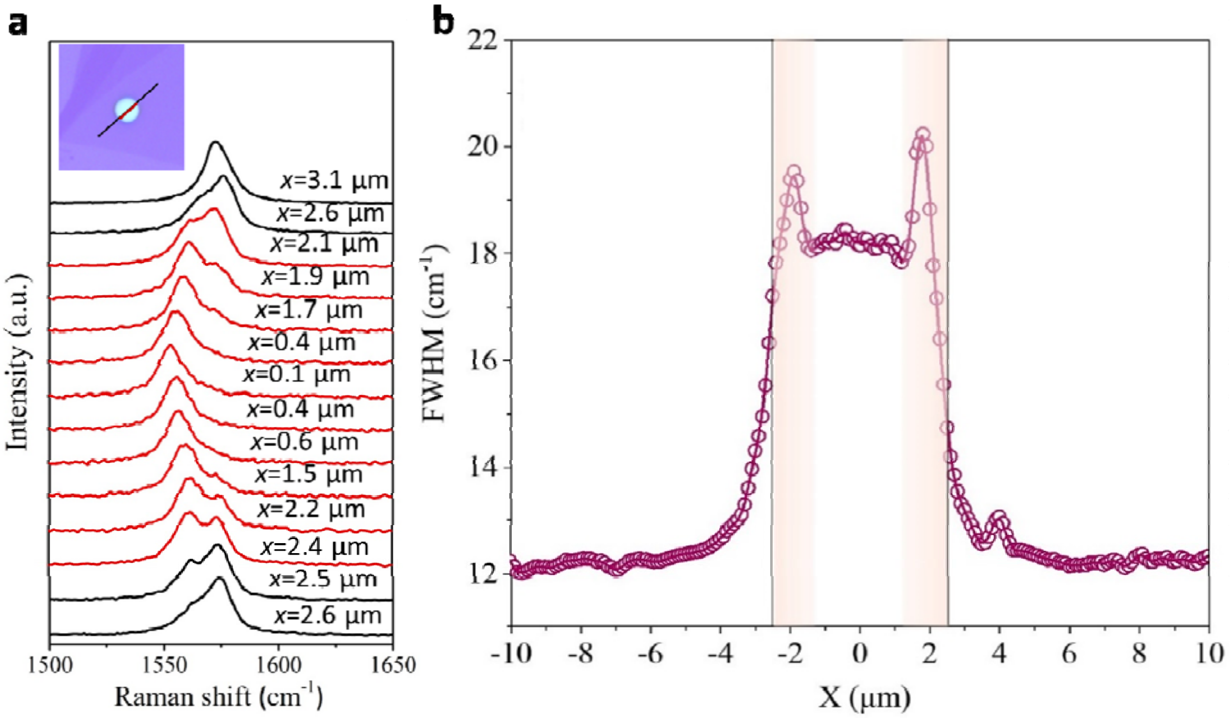

Figure S10 | Line mapping of the width of Raman G band. (**a**) For a SiO_2-supported graphene bubble at *h/a*= 0.074, a series of Raman spectra (G band) are stacked vertically in the direction of the line scan. The x is defined by the distance to the center of the hole (the bubble). Substantial variations in both the frequency and the full width at half-maximum (FWHM) can be detected. The apparent downshift of Raman G band has been shown in Figure S9. The peak broadening at the edge ( ) and the sharpening at the center ( ) of the hole are highlighted. (**b**) We further quantitatively illustrate the FWHM as a function of the radius location. Solid vertical lines are positioned at the edges of the bubble. We note that:

i) Raman peak width mainly relies on the lattice deformations and is regarded as a measure of strain distribution in graphene. Typically, the full width at half-maximum (FWHM) of graphene on a substrate is ranging from 11.5-14 cm^{-1} [4,6]. In Figure S10, we find that the formation of the suspended graphene bubble obviously enhance the FWHM of G band, especially near the edge of the hole (up to 20 cm^{-1}).

ii) The broadening behavior of the G band FWHM is a result of so-called convoluting shifted peaks from the almost unstrained region (substrate-supported graphene) and highly strained region (suspended graphene) [7]. The FWHM starts broadening inside the hole because of the ~1 µm size of the laser spot. In other words, when the laser is focused on the suspended graphene that is close to the edge, signals from both suspended graphene and supported graphene may be detected. These two signal components add up, yielding a non-Lorentzian shape with relatively large width. Such fact may also contribute to the deviation between predicted Raman shifts by our theory and measured by experiments, especially near the edge of graphene bubbles.

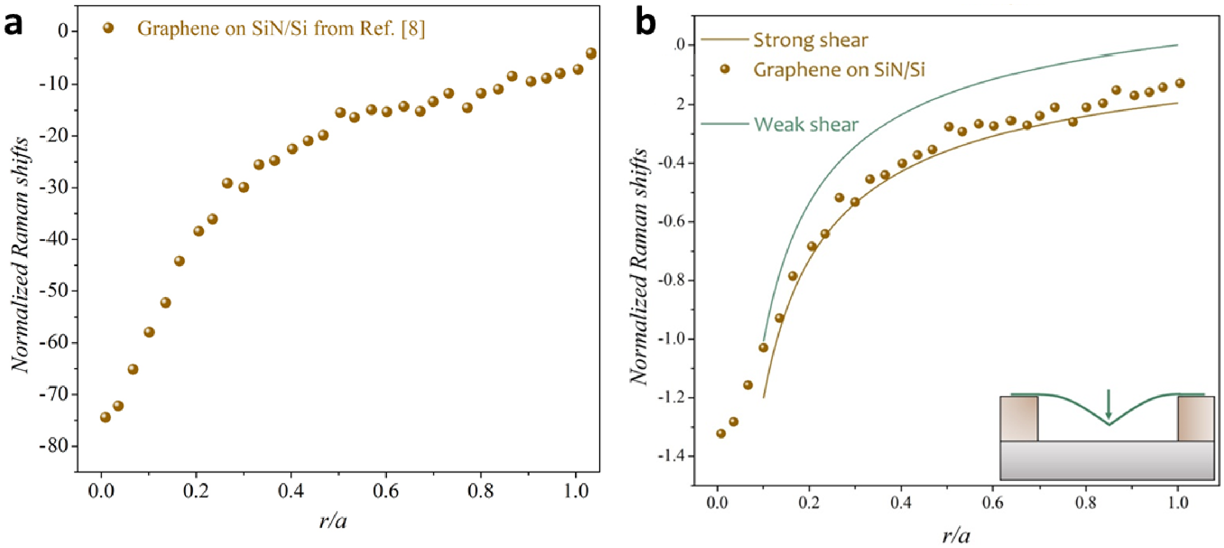

Figure S11 | (**a**) Raman shifts of the 2D band of a multilayer graphene tent as a function of *r/a* (from K. Elibol et al. [8]). Like that in bubbles, *r* is defined by the distance to the center of the tent and *a* is the radius of the tent. (**b**) Normalized Raman shifts predicted by our analytical solution (solid curves) and measured by experiments [8]. Following the same strategy outlined for the bubbles, we plotted the measured and predicted 2D band shifts for strong- - neisen parameter for the 2D band shift of the multilayer graphene [9]. The shear deformation potential term in Eq. (6) was neglected since the is not well-characterized for multilayer graphene and it neisen parameter term under biaxial stress state.

Supplementary Material Note 3

In main text, we have the explicit radius and circumferential strain fields with the sliding displacement to be determined:

$$\varepsilon_r = \begin{cases} \beta\frac{h^2}{a^2}\left(1-\frac{1+\nu-2\alpha\nu}{2\alpha-1-\nu}\left(\frac{r}{a}\right)^{2\alpha-2}\right)+\frac{u_s}{a},\ r \le a \\ -\frac{au_s}{r^2},\ r > a \end{cases} \quad \text{(1a)},$$

$$\varepsilon_\theta = \begin{cases} \beta\frac{h^2}{a^2}\left(1-\left(\frac{r}{a}\right)^{2\alpha-2}\right)+\frac{u_s}{a},\ r \le a \\ \frac{au_s}{r^2},\ r > a \end{cases} \quad \text{(1b)}.$$

To determine u_s in terms of the out-of-plane deformations of the blister, we consider the weak-shear limit, where the membrane in the annular region outside of the blister edge ($r > a$) slides inward. With zero shear stress at the frictionless interface between the membrane and the substrate, the stress and displacement in the annular region can be obtained as the classical Lamé problem in linear elasticity [9]. The radial and circumferential components of the membrane stress are:

$$N_r = \frac{C_1}{r^2} + C_2 \quad \text{(2a)},$$

$$N_\theta = -\frac{C_1}{r^2} + C_2 \quad \text{(2b)},$$

where $N_r = \sigma_r t$ and $N_\theta = \sigma_\theta t$; σ_r and σ_θ are, respectively, the radial and circumferential stresses; and t is the membrane thickness. Correspondingly, the radial displacement is

$$u = \frac{1}{E_{2D}}\left[-\frac{(1+\nu)C_1}{r} + C_2(1-\nu)r\right] \quad \text{(3)}.$$

For an infinitely large membrane, both the stress and the displacement approach zero as $r \to \infty$, which requires $C_2 = 0$. At the edge of the blister ($r = a$), the radial stress and displacement are continuous. By letting Eq. (3) be u_s at $r = a$, we obtain $C_1 = -\frac{E_{2D}au_s}{1+\nu}$. For the radial stress, we have by Hooke's law

$$N_r = \frac{E_{2D}}{1-\nu^2}(\varepsilon_r + \nu\varepsilon_\theta) \quad \text{(4)},$$

where the strain components on the right-hand side are given by Supplementary Eqs. (1a) and (1b) at $r = a$, and the radial stress on the left-hand side is given by Supplementary Eq. (2a) at $r = a$. The stress continuity then leads to

$$u_s = -\frac{\alpha(1+\nu)}{8}\frac{h^2}{a} \tag*{(5).}$$

Supplementary Material Note 4

In this section, we numerically solve the Föppl–von Kármán (FvK) equations for a circular membrane under uniform pressure (bubble) and a point load (tent). Here, we briefly introduce our modifications to a previously established finite difference method to solve for the sliding boundary case for bubbles and tents [11]. We consider the bending stiffness of the membrane and write the FvK equations in terms of the displacement [11]:

$$\frac{d^2u}{dr^2} + \frac{1}{r}\frac{du}{dr} - \frac{u}{r^2} = -\frac{1-\nu}{2r}\left(\frac{dw}{dr}\right)^2 - \frac{dw}{dr}\frac{d^2w}{dr^2} \tag*{(6),}$$

$$D\left(\frac{d^3w}{dr^3} + \frac{1}{r}\frac{d^2w}{dr^2} - \frac{1}{r^2}\frac{dw}{dr}\right) - \frac{E_{2D}}{1-\nu^2}\frac{dw}{dr}\left(\frac{du}{dr} + \nu\frac{u}{r} + \frac{1}{2}\left(\frac{dw}{dr}\right)^2\right) = \frac{1}{r}\int_0^r q(r) r dr \tag*{(7),}$$

where D is the bending rigidity of the membrane, E_{2D} is the in-plane stiffness of the membrane. The lateral loading intensity, $q(r)$, can take two forms depending on the type of load. For a bubble, $q(r)$ is a constant; for a tent, $q(r) = \frac{P\delta(r)}{2\pi r}$, where P is the magnitude of the point load and $\delta(r)$ is the Dirac delta function. We then adopt the classical relation between the bending stiffness and in-plane stiffness such that the thickness is described as $t = \sqrt{12(1-\nu^2)D/E_{2D}}$. For convenience, we normalize the FvK equations using the following dimensionless quantities: $\bar{r} = r/t$, $\bar{a} = a/t$, $\bar{u} = u/t$, $\bar{w} = w/t$, $\bar{u}_s = u_s/t$, $\bar{q}(r) = q(r)t^3/D$, and $\bar{P} = Pt/D$. We replace the deflection with the angle of rotation, $\theta = dw/dr$, such that Eq. (6) and Eq. (7) become the following nondimensional equations:

$$g = \frac{d^2\bar{u}}{d\bar{r}^2} + \frac{1}{\bar{r}}\frac{d\bar{u}}{d\bar{r}} - \frac{\bar{u}}{\bar{r}^2} + \frac{1-\nu}{2\bar{r}}\theta^2 + \theta\frac{d\theta}{d\bar{r}} = 0 \tag*{(8),}$$

$$f = \frac{d^2\theta}{d\bar{r}^2} + \frac{1}{\bar{r}}\frac{d\theta}{d\bar{r}} - \frac{\theta}{\bar{r}^2} - 12\theta\left(\frac{d\bar{u}}{d\bar{r}} + \nu\frac{\bar{u}}{\bar{r}} + \frac{\theta^2}{2}\right) - \frac{1}{\bar{r}}\int_0^{\bar{r}} \bar{q}(r)\bar{r} d\bar{r} = 0 \tag*{(9).}$$

Following the finite difference method, we discretize the equations with $\Delta\bar{r} = \bar{a}/n$ and $\bar{r}_k = k\Delta\bar{r}$ for $k = 0$ to n. At each internal node ($k = 1$ to $n - 1$), we have

$$g_k = \frac{n^2}{\bar{a}^2}\left(1 + \frac{1}{2k}\right)\bar{u}_{k+1} - \frac{n^2}{\bar{a}^2}\left(2 + \frac{1}{k^2}\right)\bar{u}_k + \frac{n^2}{\bar{a}^2}\left(1 - \frac{1}{2k}\right)\bar{u}_{k-1} + \frac{1-\nu}{2k\bar{a}}\theta_k^2 + \frac{n}{2\bar{a}}\theta_k(\theta_{k+1} - \theta_{k-1}) \tag*{(10),}$$

$$f_k = \frac{n^2}{\bar{a}^2}\left(1 + \frac{1}{2k}\right)\theta_{k+1} - \frac{n^2}{\bar{a}^2}\left(2 + \frac{1}{k^2}\right)\theta_k + \frac{n^2}{\bar{a}^2}\left(1 - \frac{1}{2k}\right)\theta_{k-1} - \frac{6n}{\bar{a}}(\bar{u}_{k+1} - \bar{u}_{k-1}) - \frac{12\nu n}{k\bar{a}}\theta_k\bar{u}_k - 6\theta_k^3 - \zeta_k = 0 \tag*{(11),}$$

where ζ_k is $\bar{q}k\bar{a}/2n$ for the bubble and is $\bar{P}n/(2\pi k\bar{a})$ for the tent. The boundary conditions are $\theta_0 = \theta_n = 0, \bar{u}_0 = 0, \bar{u}_0 = \bar{u}_s$. In calculations, $\bar{u}_s$ is a prescribed but not arbitrary quantity. For each given $\bar{u}_s$, the load $\bar{P}$ needs to be solved by matching the boundary conditions at the edge: $\bar{u}_s = 0$ for a clamped interface; the displacement and radial stress component are continuous across the edge for a sliding interface. The Newton-Raphson method was used to solve Supplementary Eqs. (10) and (11). The analytical plate solution was used to provide the initial guess for the bubble, while Schwerin's classic solution was used for the tent:

$$\theta_k^{(0)}{}_{bubble} = \frac{\bar{q}k}{16n}\left(\frac{k^2}{n^2} - 1\right) \tag*{(12),}$$

$$\theta_k^{(0)}{}_{tent} = -\frac{2}{3}\left(\frac{\bar{P}n}{4\pi(1-\nu^2)\bar{a}k}\right)^{\frac{1}{3}} \tag*{(13),}$$

and $\bar{u}_k^{(0)} = 0$. We successively iterate until the convergence condition is satisfied. At each iteration, the residuals are calculated by Supplementary Eqs. (12) and (13) at each internal node, and the correction vector is calculated as

$$\begin{pmatrix}\Delta\boldsymbol{\theta}\\ \Delta\bar{\boldsymbol{u}}\end{pmatrix} = -\begin{bmatrix}\frac{\partial\boldsymbol{f}}{\partial\boldsymbol{\theta}} & \frac{\partial\boldsymbol{f}}{\partial\bar{\boldsymbol{u}}}\\ \frac{\partial\boldsymbol{g}}{\partial\boldsymbol{\theta}} & \frac{\partial\boldsymbol{g}}{\partial\bar{\boldsymbol{u}}}\end{bmatrix}^{-1}\begin{pmatrix}\boldsymbol{f}\\ \mathbf{g}\end{pmatrix} \tag*{(14),}$$

where $\Delta\boldsymbol{\theta}$ is a vector of *n*-1 components ($\Delta\boldsymbol{\theta}_k$, $k = 1$ to $n - 1$) and same for $\Delta\bar{\boldsymbol{u}}$, $\boldsymbol{f}$, and $\boldsymbol{g}$. The Jacobian matrix on the right-hand side of Eq. (14) consists of four square blocks, each with a rank of *n*-1. This matrix can be readily constructed from Supplementary Eqs. (10) and (11). For the convergence criterion, we require that the L2-norm of the relative correction vector is smaller than 10^{-4}, *i.e.* 1% accuracy. If the convergence criterion is not satisfied, the iteration procedure then repeats with a new approximation, $\theta_k^{(i+1)} = \theta_k^{(i)} + \Delta\theta_k$ and $\bar{u}_k^{(i+1)} = \bar{u}_k^{(i)} + \Delta\bar{u}$.

Subsequently, we calculate the deflection at each node by numerical integration:

— (15)

for to , and . In Fig. S1, we plotted the calculated deflection normalized by the center deflection (. The strain components at each node can also be calculated as

— — (16),

— (17),

for to . At the center, —. Note that at the edge, we can have — and —, due to the continuity of radial stress and displacement across the edge.

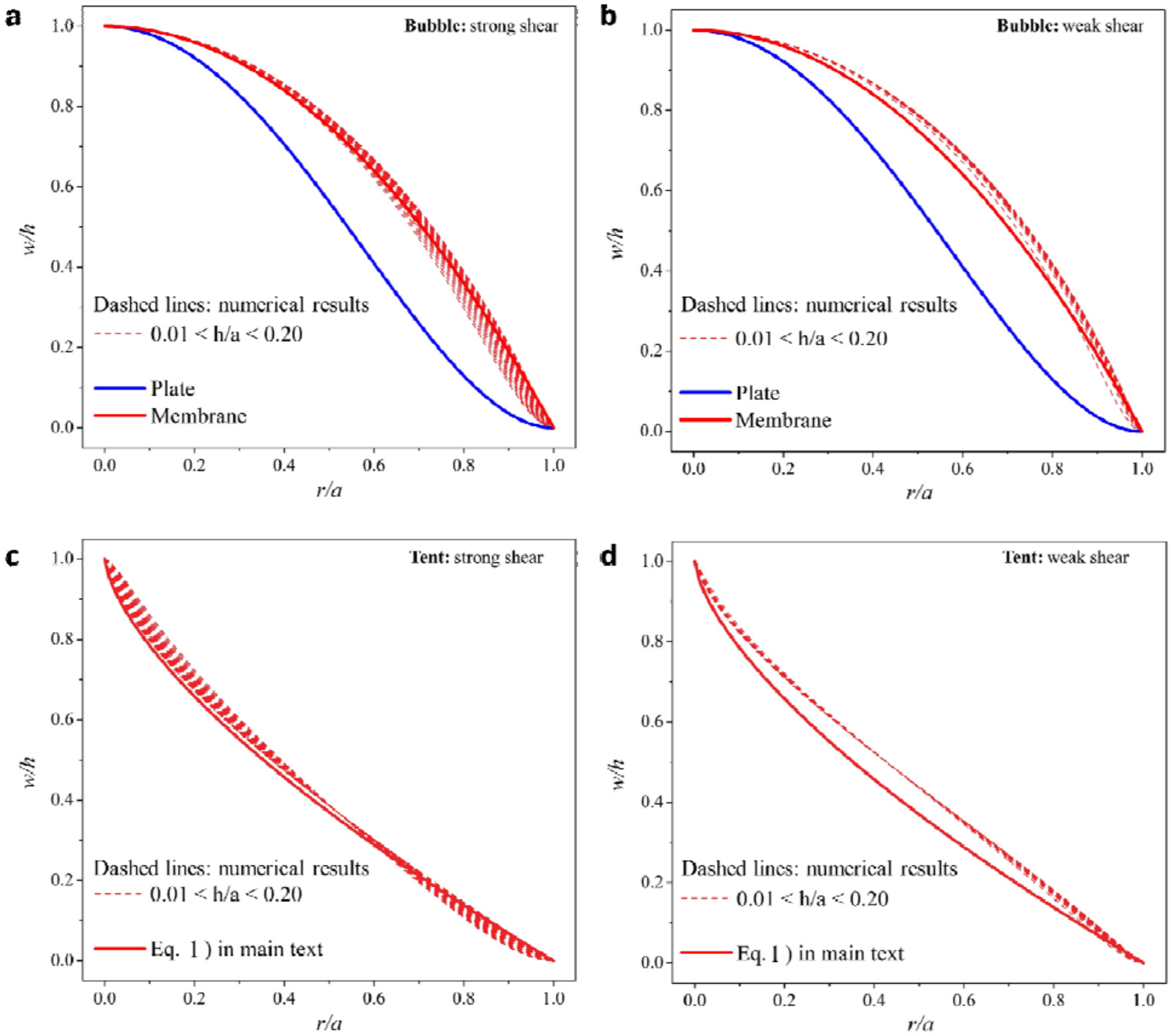

Figure S12 | Out-of-plane deformations in 2D material blisters. Normalized deflection curves predicted by our theoretical solution (solid lines) and solved by numerical analysis (dash lines) for the bubble (**a, b**) and tent (**c, d**), subject to both clamped, strong and frictionless, sliding interfaces. The deflection curve is normalized by the center deflection. The numerical result is solved for a monolayer graphene with $a = 200$ nm and $0.01 < h/a < 0.2$.

Supplementary Material Note 5

In main text, we derived a scaling law by considering the balance between adhesion and strain energy in a bubble or a tent:

$$h/a = (\phi \Delta\gamma / E_{2D})^{1/4} \quad (18).$$

The prefactor, ϕ, can be obtained by minimizing the total energy. The total energy of the system U_{total} consists of the following three energy terms:

$$U_{total} = U_E + U_I + U_P \quad (19),$$

where U_e is the elastic strain energy of the membrane, U_i is the interface adhesion energy between the membrane and the substrate, and U_p is the potential energy associated with the blister contents. We can now derive the elastic strain energy by Eq. (4) from the main text, consisting of two parts, one due to stretching and the other due to bending. According to our numerical results, the bending effects can reasonably be neglected for our experimentally observed blisters. The elastic stretching energy per unit area of the membrane is

$$U_s(r) = \frac{E_{2D}}{2(1-\nu^2)}(\varepsilon_r{}^2 + 2\nu\varepsilon_r\varepsilon_\theta + \varepsilon_\theta{}^2) \quad (20),$$

This leads to the strain energy of a blister in the present study:

$$U_E = 2\pi \int_0^a U_S(r)\, rdr + 2\pi \int_a^\infty U_S(r)\, rdr \quad (21),$$

where the first term represents the strain energy in the laterally loaded membrane, and the second term is a result of interface sliding (which is negligible for the strong-shear limit).

The adhesion energy required to form the blister is simply the energy change per unit area, $\Delta\gamma$, multiplied by the blister area,

$$U_I = \pi a^2 \Delta\gamma \quad (22),$$

where we assume that the change in contact area due to the deformation is negligible since it scales as $a^2\boldsymbol{O}(h^2/a^2)$.

The last term in the Supplementary Eq. (19) is the potential energy associated with contents, which is to be determined according to the interface confining conditions. For a liquid-filled bubble and a post-supported tent, $U_P = 0$. For a bubble filled with ideal gas, U_P follows the ideal gas law. Here, we derive ϕ for the six different scenarios with differing interfacial shear conditions and interfacial contents.

i) *Liquid-filled bubbles with a strong-shear interface*. The membrane outside the bubble edge does not deform and confined liquid does not contribute to U_P due to its incompressibility. The total free energy for the bubble is then obtained as a function of two kinematic parameters by explicitly rewriting Supplementary Eq. (19) as

$$U_{total}(a) = \frac{2(7-\nu)E_{2D}V^4}{3\pi^3(1-\nu)a^{10}} + \pi a^2 \Delta\gamma \quad (23),$$

where $V = \frac{\pi}{2}a^2 h$, due to the Eq. (1) with $\alpha = 2$ from the main text, is the volume of the interface confined liquid. Given the incompressible V, the first term on the right-hand side of Supplementary Eq. (23) is the elastic strain energy in the membrane, which decreases with increasing the bubble radius a. The second term stems from the change of interface energy, which increases with increasing bubble radius. The competition between the two terms leads to an equilibrium bubble radius that minimizes the total free energy, namely

$$\left(\frac{\partial U_{total}}{\partial a}\right)_V = 0 \quad (24),$$

which gives rise to Eq. (18) with $\phi = \frac{24(1-\nu)}{5(7-\nu)}$.

ii) *Liquid-filled bubbles with a weak-shear interface*. The elastic strain energy outside the bubble has to be considered due to the interfacial sliding. Following Supplementary Eqs. (19) – (23), the total free energy is obtained as

$$U_{total}(a) = \frac{8E_{2D}V^4}{3\pi^3 a^{10}} + \pi a^2 \Delta\gamma \quad (25).$$

Similarly, $\left(\frac{\partial U_{total}}{\partial a}\right)_V = 0$ gives rise to Eq. (18) with $\phi = \frac{6}{5}$.

iii) *Gas-filled bubbles with a strong-shear interface.* In this case, the isothermal expansion of fixed number of interface confined gas molecules (N) contributes to the potential energy:

$$U_p = \int_{V(p)}^{V(p_0)} p dV \quad (26),$$

where $V(p)$ is the volume of an ideal gas under current pressure p and $V(p_0)$ is the volume of an ideal gas under atmospheric pressure. The pressure and volume of the ideal gas are assumed to follow the ideal gas law, which behaves as a constraint when minimizing the total energy of the system:

$$NkT = pV \simeq \frac{\pi(7-\nu)}{6(1-\nu)}\frac{E_{2D}h^4}{a^2}, \tag{27}$$

where k is Boltzmann constant and T is temperature, and the right-hand side relation is readily obtained by minimizing the potential energy of the uniformly pressurized membrane [12]. By combining Supplementary Eqs. (19) – (22) with Supplementary Eq. (27), we write the total free energy in terms of only two kinematic parameters (N, a):

$$U_{total}(a) = \frac{NkT}{4} - NkT\ln Aa^{2/5} + \pi a^2 \Delta\gamma \tag{28}$$

where A is a constant related to the reference state of gas in ambient condition. The first term on the right-hand side of Supplementary Eq. (28) is the elastic strain energy in the membrane, which is independent of both the bubble radius and height under constant N. The second term is the potential energy of the gas which decreases with increasing bubble radius, a. Meanwhile, the interfacial energy term increases as part of graphene is detached from the substrate. The competition of the last two terms leads to an equilibrium bubble radius when the total free energy is minimized such that

$$\left(\frac{\partial U_{total}}{\partial a}\right)_N = 0 \tag{29}$$

Supplementary Eq. (29) thus gives rise to

$$\Delta\gamma = \frac{5NKT}{4\pi a^2} \tag{30}$$

By plugging Supplementary Eq. (27), we derive $\phi = \frac{24(1-\nu)}{5(7-\nu)}$ for Supplementary Eq. (17), which is also the case for liquid-filled bubbles with a strong-shear interface.

iv) *Gas-filled bubbles with a weak-shear interface.* When interface sliding occurs, Eq. (27) becomes

$$NkT = pV \simeq \frac{2\pi}{3}\frac{E_{2D}h^4}{a^2} \qquad (31).$$

After combining Eqs. (19-22) and Eq. (31), we find that Eqs. (28-30) still work for the gas-filled bubbles with a weak-shear interface. Then combining Eq. (30) and Eq. (31) gives us $\phi = \frac{6}{5}$, which also applies to liquid-filled bubbles with a weak-shear interface.

v) *Tents with a strong-shear interface.* The tent can be treated as a displacement-controlled delamination experiment where the height is fixed and U_P is zero. From Supplementary Eqs. (18) – (21), the total energy of a tent with clamped boundaries is

$$U_{total}(a) = \frac{\pi(5-3\nu)E_{2D}h^4}{72(1-\nu)a^2} + \pi a^2 \Delta\gamma \qquad (32).$$

Clearly, the competition between the elastic strain energy and the interface energy leads to

$$\left(\frac{\partial U_{total}}{\partial a}\right)_h = 0, \qquad (33),$$

which gives rise to Eq. (18) with $\phi = \frac{72(1-\nu)}{5-3\nu}$.

vi) *Tents with a weak-shear interface.* The elastic strain energy outside the tent is considered. Following Supplementary Eqs. (19) – (22), the total energy is then obtained:

$$U_{total}(a) = \frac{\pi E_{2D}h^4}{18a^2} + \pi a^2 \Delta\gamma \qquad (34).$$

Similarly, $\left(\frac{\partial U_{total}}{\partial a}\right)_h = 0$ which gives rise to Eq. (18) with $\phi = 18$.

[1] C. J. Brennan, R. Ghosh, K. Koul, S. K. Banerjee, N. Lu, and E. T. Yu, *Nano Lett***.** **17**, 5464 (2017).
[2] R. Frisenda, E. Navarro-Moratalla, P. Gant, D. Perez De Lara, P. Jarillo-Herrero, R. V. Gorbachev, and A. Castellanos-Gomez, *Chem. Soc. Rev.* **47**, 53 (2018).
[3] Y. Zhang, C. Hui, R. Sun, K. Li, K. He, X. Ma, and F. Liu, *Nanotechnology* **25**, 135301 (2014).
[4] L. G. Cancado *et al.*, *Nano Lett.* **11**, 3190 (2011).
[5] J. E. Lee, G. Ahn, J. Shim, Y. S. Lee, and S. Ryu, *Nat. Commun.* **3**, 1024 (2012).
[6] A. C. Ferrari, *Solid State Commun*. **143**, 47 (2007).
[7] C. Metzger *et al*, *Nano Lett.* **10**, 6 (2009).
[8] K. Elibol, B. C. Bayer, S. Hummel, J. Kotakoski, G. Argentero, and J. C. Meyer, *Sci. Rep.* **6**, 28485 (2016).

[9] Z. H. Ni, T. Yu, Y. H. Lu, Y. Y. Wang, Y. P. Feng, and Z. X. Shen, *ACS Nano* **2**, 2301 (2008).
[10] M. H. Sadd, *Elasticity: theory, applications, and numerics* (Academic Press, 2009).
[11] P. Wang, W. Gao, Z. Y. Cao, K. M. Liechti, and R. Huang, *J. Appl. Mech*. **80**, 040905 (2013).
[12] K. M. Yue, W. Gao, R. Huang, and K. M. Liechti, *J. Appl. Phys*. **112**, 083512 (2012).